



**Rashba-split surface state and spin-dependent photon emission from Re(0001) at  $\bar{\Gamma}$** Sven Schemmelmann <sup>1,\*</sup>, Peter Krüger,<sup>2</sup> Fabian Schöttke,<sup>1</sup> and Markus Donath <sup>1,†</sup><sup>1</sup>*Physikalisches Institut, Westfälische Wilhelms-Universität Münster, Wilhelm-Klemm-Straße 10, 48149 Münster, Germany*<sup>2</sup>*Institut für Festkörpertheorie, Westfälische Wilhelms-Universität Münster, Wilhelm-Klemm-Straße 10, 48149 Münster, Germany*

(Received 26 July 2021; revised 25 September 2021; accepted 4 November 2021; published 18 November 2021)

The unoccupied electronic structure of the Re(0001) surface is investigated by spin- and angle-resolved inverse photoemission, experimentally and theoretically. The work is focused on the states around the center of the surface Brillouin zone  $\bar{\Gamma}$ , where a hole pocket of a surface state with Rashba-type spin splitting is detected. Furthermore, we observe spin-dependent photon emission from unpolarized surface and bulk states at  $\bar{\Gamma}$ . The size and sign of the spin asymmetry depends on experimental parameters such as the direction of the electron spin polarization and the photon detection angle. Maximum (zero) spin asymmetry is detected if the electron spin polarization and the plane of photon emission are perpendicular (parallel). The effect is traced back to spin-orbit-induced hybridization of the involved states.

DOI: [10.1103/PhysRevB.104.205425](https://doi.org/10.1103/PhysRevB.104.205425)**I. INTRODUCTION**

Spin-orbit-induced photoelectron spin polarization from nonmagnetic samples has been studied for about three decades with continuing interest and fascinating outcome until this day [1–3]. One research focus is the determination of the intrinsic spin polarization of the states under investigation. However, there are also extrinsic effects that influence the spin polarization of the emitted and detected photoelectrons caused by the matrix elements of the optical transition, where not only the initial state but also the final state as well as experimental parameters such as light polarization and sample orientation enter. The same is true for inverse photoemission, the time-reversed process, which is used to investigate the unoccupied electronic states above the Fermi level [4]. As a consequence, another research focus developed, where the influence of the experimental conditions on the experimentally obtained spin information is examined in detail. In particular, states with mixed orbital symmetries are candidates for spin effects in experiment different from the intrinsic spin polarization [5–10]. Even at high-symmetry points such as points with time-reversal invariant momenta, spin effects can occur [11].

A wealth of information has been gathered about the metals of the sixth period of the periodic table with high atomic number and, as a consequence, considerable spin-orbit-coupling (SOC): Ta and W with body-centered-cubic structure and Ir, Pt, and Au with face-centered-cubic structure. The two elements in between, Re and Os with hexagonal-closed-packed (hcp) structure, have been almost slighted so far. At the surface of all these materials, the broken inversion symmetry in combination with SOC leads to spin splittings of electronic states. This effect is called Rashba effect [12] and has been

verified at several surfaces, first of all at the prototypical *sp*-type surface state in the *L* gap of Au(111) [13–16]. Ta and W exhibit *d*-derived spin-dependent surface states from Rashba-like states to even topologically protected states with linear dispersion and helical spin texture [17–21]. For hcp Re(0001), recent experiments detected a Rashba-split surface state in the occupied band structure that crosses the Fermi energy near the  $\bar{\Gamma}$  point and is predicted to have a hole pocket around  $\bar{\Gamma}$  [22].

In this paper, we study the spin-dependent unoccupied electronic structure of Re(0001) around  $\bar{\Gamma}$  with spin- and angle-resolved inverse photoemission (IPE) and theoretical calculations for the band structure as well as for the IPE spectra. Our motivation is twofold. First, we want to detect the unoccupied part of the surface state and reveal its intrinsic spin structure. Second, we aim at testing theoretical predictions for extrinsic spin effects in measurements of unpolarized states at  $\bar{\Gamma}$  by varying experimental parameters: rotating the spin polarization of the incoming electrons and using several photon detectors positioned at different angles with respect to the sample. For fcc(111) surfaces at  $\bar{\Gamma}$ , spin effects are predicted for states with mixed orbital symmetries [5]. We can apply this work to hcp(0001) because the bands with wave vector perpendicular to the surface have also  $\Lambda$  symmetry. A detailed analysis of the symmetry of the involved states allows us to understand the spin-dependent photon emission obtained from unpolarized states at Re(0001)- $\bar{\Gamma}$ .

**II. EXPERIMENT**

All experiments have been performed in an ultrahigh-vacuum apparatus with a base pressure of  $<5 \times 10^{-11}$  mbar. The unoccupied electronic states have been investigated via spin- and angle-resolved IPE [23]. For excitation, we used a rotatable spin-polarized electron source (ROSE) based on photoemission from GaAs with a spin polarization *P* of 29% [24]. For normal electron incidence on the sample, the

\*sven.schemmelmann@uni-muenster.de

†markus.donath@uni-muenster.de

in-plane spin polarization can be rotated freely. In addition, the polar and azimuthal angles of the sample can be varied. The emitted photons from optical transitions into unoccupied states are detected by several bandpass detectors, all with a detection energy of  $\hbar\omega = 9.9$  eV [25], yet positioned at different detection angles as described in Ref. [26] and sketched in Figs. 3 and 4. C1 is located at an angle of  $70^\circ$  within the measuring plane on one side of the electron beam, while the measuring plane is spanned by the electron beam and the surface normal. C2 is located at an angle of  $35^\circ$  out of the measuring plane, symmetrically with respect to positive and negative  $\theta$ . C3 is located at an angle of  $65^\circ$  in and  $32^\circ$  out of the measuring plane (i.e.,  $69^\circ$  with respect to the electron beam) on the other side of the electron beam compared with C1. For negative angles  $\theta$ , the surface normal is rotated towards C1. For positive angles, the sample is rotated in the opposite direction towards C3, whereby it should be noted that C3 is not located within the measuring plane. The overall energy resolution of the setup is about 400 meV, while the angular resolution of the electron beam is  $\Delta\theta = 3^\circ$  [24,27]. The electron beam is about 2 mm in diameter.

The Re(0001) sample was obtained from MaTeCK GmbH (Germany). The surface was cleaned by cycles of heating in an oxygen atmosphere ( $3 \times 10^{-8}$  mbar) at 1400 K and subsequent flashing to 1800 K [28]. The surface quality was evaluated by Auger electron spectroscopy, with a small to vanishing carbon signal as sensitive criterion for cleanness, and by low-energy electron diffraction (LEED) for crystalline order at the surface. LEED experiments revealed that the surface persists of stripelike crystallites with a width of about 2 mm and tilt angles up to  $1^\circ$  between two crystallites. As a consequence, a LEED map of the sample surface was generated in order to find large single-oriented crystallites having a small tilt angle to neighboring crystallites of less than  $0.5^\circ$ , which is well below the angular resolution of our IPE setup. All IPE experiments were performed at room temperature on parts of the sample surface meeting the described criteria.

### III. THEORY

We employ density-functional theory (DFT) with the local-density approximation (LDA) [29] to obtain the ground-state properties of the system. These calculations [30] are performed employing nonlocal norm-conserving pseudopotentials in the separable Kleinman-Bylander form [31] including scalar-relativistic corrections and spin-orbit coupling (SOC) [32]. The electronic wave functions are represented by Gaussian orbitals with  $s$ ,  $p$ , and  $d$  symmetries and decay constants of 0.10, 0.35, and 1.07 (in atomic units) for each symmetry type. The Re(0001) surface is described within the supercell approach. We use a slab of 40 Re layers and a vacuum of 22 Å is employed to decouple neighboring slabs. In structure optimizations, the outmost eight layers are allowed to relax. Brillouin zone integrations are carried out using a  $12 \times 12 \times 1$  Monkhorst-Pack mesh [33] for the slab calculations. In the case of bulk Re, a mesh of  $12 \times 12 \times 6$  points is employed.

We obtain a bulk lattice constant of  $a = 2.749$  Å and a  $c/a$  ratio of 1.621. These values are close to the results of Urru and Dal Corso [34] ( $a = 2.739$  Å,  $c/a = 1.611$ ). The

experimental findings are  $a = 2.761$  Å and  $c/a = 1.615$  [35]. In our structure optimization for Re(0001), we find a compression of the distance between the two outmost layers by 5.6% with respect to the ideal interlayer distance and an expansion by 2.5% for the distance between the second and third layer. These values are close to the results of Urru and dal Corso [34] (5.4%, 2.9%). Experimentally, there is indication that the distance between first and second atomic layer is contracted by about 5% [36]. In our calculations, the distances of the next layers turn out to be decreased by 1.8% and increased by 0.7%, respectively. The slight underestimation of the lattice constant is typical within DFT-LDA. We have also performed calculations based on the generalized gradient approximation (GGA) [37]. The resulting lattice constant of  $a = 2.809$  Å overestimates the experimental ones as expected. The results for the structural relaxations ( $-5.8\%$ ,  $+2.7\%$ ,  $-2.0\%$ ,  $+0.9\%$  changes of the distances with respect to the GGA interlayer distances) are very similar to the corresponding values obtained in DFT-LDA. The band structure resulting in DFT-GGA is also very close to that in DFT-LDA.

In addition to the supercell calculations, we have employed the scattering-theoretical method to calculate the surface band structure. This approach is also used in the simulation of the IPE by calculating the intensity for a dipole-allowed transition between the initial states with energy  $E_i$ , i.e., incoming electrons, and the final states at  $E_f$ , i.e., unoccupied Bloch states below the vacuum level. This approach solves the Kohn-Sham equations for a semi-infinite system by treating the Rhenium surface as a two-dimensionally periodic perturbation of the total system. To represent the perturbation, the wave functions inside as well as outside [38] the crystal are expanded in terms of Gaussian orbitals. The corresponding secular equation is solved by calculating its Green's function  $G$  which is energy-, wave-vector-, and spin-dependent.  $G(E_f)$  allows us to determine bound final states as well as surface resonances with high spectral resolution. The initial state  $|\psi_i\rangle$  resulting from the scattering of an incoming electron's plane wave with spin  $\mathbf{S}$  (decoded in the corresponding spinor) at the surface is deduced from  $G(E_i)$ . The calculational procedure is similar to the evaluation of ballistic electron transport [39] at the interface between two crystals. We have described the formal treatment and computational procedure of this method in Refs. [40,41].

Within the dipole approximation, the intensity  $I$  for the transition between the IPE initial and final states depends on the direction of the vector potential  $\mathbf{A}$  of the detected photons in the experimental setup

$$I(\mathbf{A}, \mathbf{S}) \sim \text{Im} \langle \psi_i(\mathbf{S}) | \mathbf{A} \cdot \nabla G(E_f) \mathbf{A} \cdot \nabla | \psi_i(\mathbf{S}) \rangle \quad (1)$$

In our approach, all wave functions and operators are represented in a Gaussian basis. To account for the decay of the initial states due to many-body effects, a potential with an imaginary part of 1.0 eV inside the Re crystal is employed in the calculation of  $G(E_i)$ . Due to the decay of the initial states into the crystals and the decay of the final states into the vacuum, a numerically converged evaluation of Eq. (1) is achieved by considering contributions from orbitals localized in a region of 44 Å inside the crystal and 22 Å above the surface.

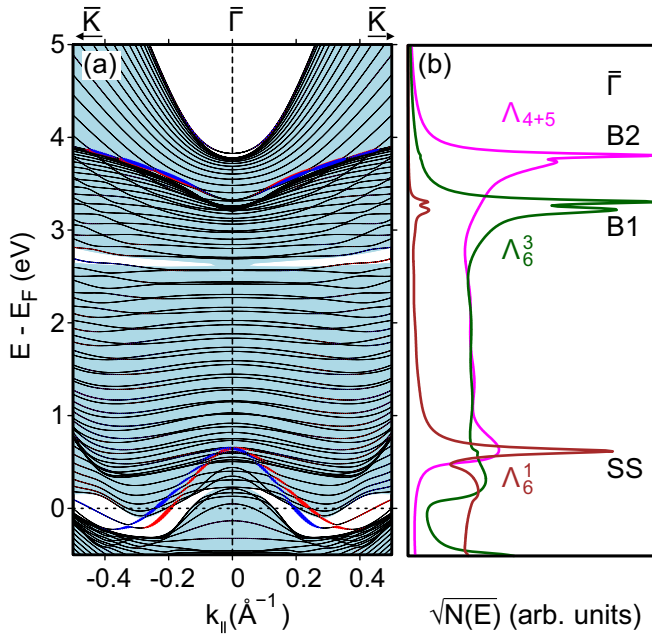


FIG. 1. (a) Density-functional-theory calculations of the band structure of Re(0001) along  $\bar{\Gamma}\bar{K}$ : surface-projected bulk-band structure (blue shaded areas), slab calculation (black solid lines), spin-dependent surface-derived state around the Fermi energy (red and blue dots, size of symbols represents spin polarization of up to about 85%). (b) Orbital decomposition of bands at the  $\bar{\Gamma}$  point (square root of density of states) for the different double-group symmetries  $\Lambda_{4+5}$ ,  $\Lambda_6^3$ , and  $\Lambda_6^1$ . The square root is used to show the small components of the densities of states, in particular the  $\Lambda_6^1$  part of B1, more clearly. All curves are broadened by 20 meV.

## IV. RESULTS AND DISCUSSION

### A. Rashba-split surface state

Figure 1(a) presents a DFT calculation of the projected electronic band structure of Re(0001) in the  $\bar{\Gamma}\bar{K}$  direction around the  $\bar{\Gamma}$  point. Black lines are results of the slab calculation; blue-shaded areas show surface-projected bulk bands. Surface states are represented by blue- and red-dotted lines, where the dot size denotes the expectation value of the electron spin polarization. A rather large band gap opens above 4 eV, in which—in experiment—an image-potential-induced surface state (IS) is observed, which is, however, not described by a DFT calculation. Another band gap is visible between 0.1 and  $0.5 \text{ \AA}^{-1}$  below the Fermi energy, which hosts a surface state SS, showing a Rashba splitting with spin polarization values of up to about 85%. This state crosses the Fermi energy and becomes unoccupied around  $\bar{\Gamma}$ , where no gap exists anymore for this state. These findings agree with former theoretical work [34].

Figure 1(b) shows the density of states at  $\bar{\Gamma}$  in the first six atomic layers decomposed for different double group symmetries. SS has mainly  $\Lambda_6^1$  symmetry with contributions of  $\Lambda_6^3$  and  $\Lambda_{4+5}$  symmetries. Beside SS, two additional features B1 at 3.2 eV and B2 at 3.8 eV stand out. B1 has mainly  $\Lambda_6^3$  symmetry, some contributions of  $\Lambda_{4+5}$  and only small contributions of  $\Lambda_6^1$ , whereas B2 has almost pure  $\Lambda_{4+5}$  character. Note that B1 and B2 consist of two peaks separated by about

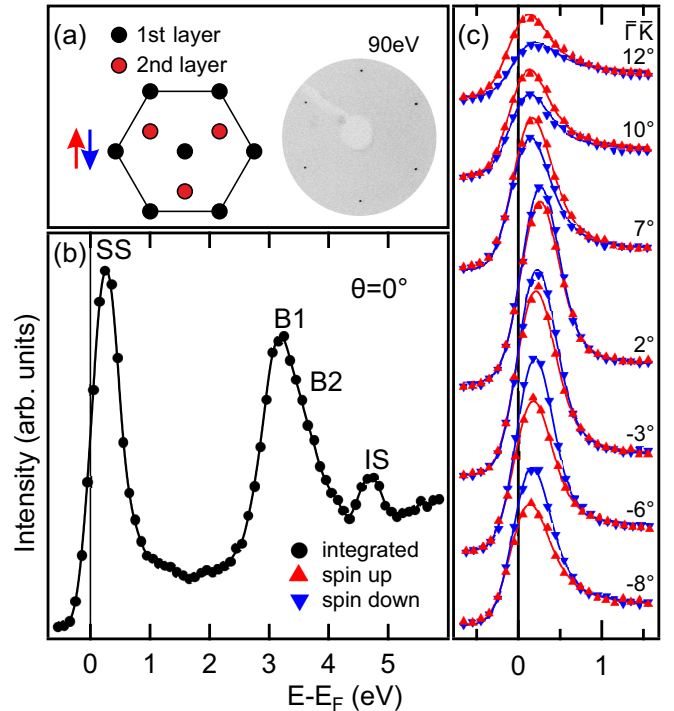


FIG. 2. (a) Scheme of the atom positions in the first two layers of Re(0001) and LEED pattern. (b) Spin-integrated IPE spectrum for normal electron incidence (sum over several counters). (c) Spin-resolved IPE spectra of the surface state SS for various angles of electron incidence  $\theta$  along  $\bar{\Gamma}\bar{K}$ , obtained with counter C3. For positive angles of incidence, the intensity for spin-up electrons dominates the spectra, while spin down dominates for negative angles.

100 meV. For both states, the high-energy peaks are surface related, while the contributions at lower energies represent bulk states.

The unoccupied part of the surface state is expected to appear within 0.5 eV above the Fermi energy. As a consequence, the finite energy resolution of IPE will influence the experimental observation with respect to peak positions and intensities [42]. At normal electron incidence, no splitting and, thus, no spin-dependent spectral intensity is predicted. For positive  $k_{\parallel}$ , the surface-state branch with spin-down polarization (blue) is lower in energy than spin up (red), resulting in lower intensity for spin down in comparison with spin up due to the Fermi level cutoff. For negative  $k_{\parallel}$ , this behavior is reversed so that spin down should have higher intensity than spin up.

Figure 2(a) shows a scheme of the sample geometry and a LEED pattern of Re(0001) representing the reciprocal space. Due to the second atomic layer with B atoms below the surface layer with A atoms, the sixfold symmetry is broken and a threefold symmetry remains. At variance with this expectation, the threefold symmetry cannot be observed in the LEED pattern of this hcp(0001) surface, which is in contrast to fcc(111) surfaces. Since a real sample surface has always (one-atomic) steps and terraces, A and B atoms are forming the topmost layer alternately in a random fashion. As a consequence, an apparent sixfold symmetry arises in the LEED patterns.

Figure 2(b) presents a spin-integrated IPE spectrum for normal electron incidence, where the data have been obtained by a summation over several counters. The spectrum shows four different states. The feature just above the Fermi energy with high intensity, which reacts sensitively to surface contamination, originates from the surface state SS, the peak at 4.75 eV is attributed to an image-potential-induced surface state IS. The spectral feature in between the two surface states consists of two contributions B1 at 3.15 eV and B2 at 3.7 eV that are not clearly resolved experimentally. B1 and B2 are attributed to the bands predicted in Fig. 1(b) and, therefore, labeled accordingly. The parabolic  $E(k_{\parallel})$  dispersion of IS was used to calibrate normal electron incidence.

A series of spin-resolved IPE spectra of SS for various angles of electron incidence in the  $\bar{\Gamma}\bar{K}$  direction of the surface Brillouin zone is shown in Fig. 2(c).  $\theta = 10^{\circ}$  corresponds to  $k_{\parallel} = 0.2 \text{ \AA}^{-1}$  at the energy of SS. The spectra have been obtained from counter C3. The intensities are highest around normal electron incidence, while decreasing intensities are observed upon increasing positive and negative angles. No pronounced peak shifts are detected because all features appear close to the Fermi level onset within the experimental energy resolution. The maximum energy amounts to about 0.25 eV around normal electron incidence tending to lower energy for off-normal incidence. However, pronounced spin-dependent intensities are detected. For positive angles, the intensity for spin-up electrons dominates the spectra, while this behavior is reversed for negative angles. These findings match with the expectations discussed above for a Rashba-split state that disperses towards lower energy, crossing the Fermi energy and becoming occupied. In summary, we detected the empty part of the Rashba-split surface state SS around  $\bar{\Gamma}$  on Re(0001).

There is, however, one observation that challenges the simple picture discussed so far. The excess spin-down intensity for negative angles is preserved beyond normal incidence. Spin-up intensity dominates until the electrons impinge at finite positive angles. In other words, we observe spin-dependent IPE intensities of an unpolarized final state at the high symmetry  $\bar{\Gamma}$  point. This effect of spin-dependent photon emission from unpolarized states will be addressed in the following section.

### B. Spin-dependent photon emission at $\bar{\Gamma}$

To understand the, within the simple Rashba model, unexpected spin asymmetry for normal electron incidence in the IPE spectra of SS, we performed detailed IPE measurements with three counters at different positions. Figure 3 shows the spin-dependent intensities of SS at constant energy ( $E - E_F = 0.15 \text{ eV}$ ) as a function of the angle of electron incidence  $\theta$  for C1, C2, and C3. The different photon detection geometries are sketched in the upper part of the figure. The angular distribution curves (ADCs) in Fig. 3 are only symmetric with respect to  $\theta = 0$  for C2, which is located symmetrically for positive and negative  $\theta$ . C1 (C3), however, exhibits intensity asymmetries in the ADCs with higher intensities for negative (positive) angles.

Furthermore, the data for the spin asymmetry  $A = (\uparrow - \downarrow) / (\uparrow + \downarrow)$ , shown in the lower part of the figure, corroborate

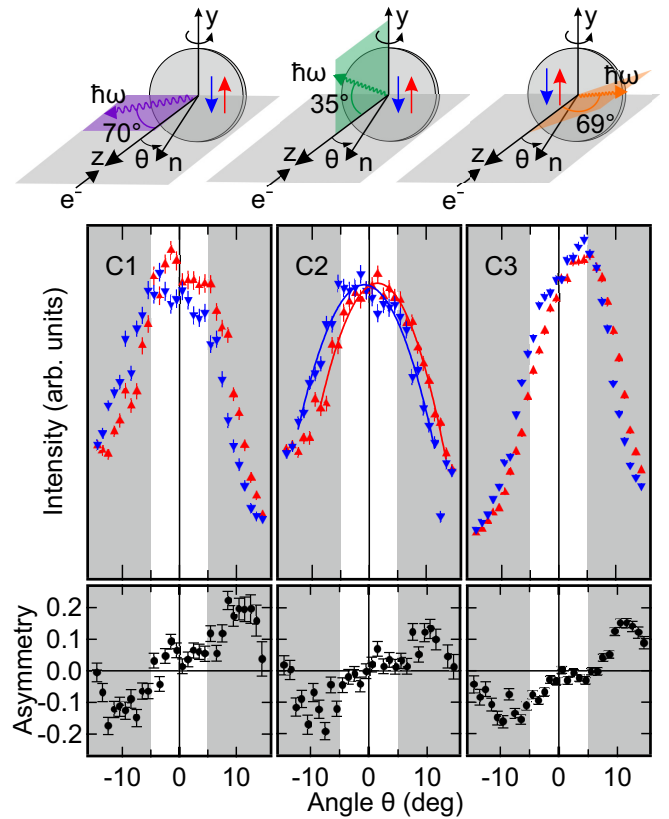


FIG. 3. Spin-resolved IPE intensities of SS at constant energy ( $E - E_F = 0.15 \text{ eV}$ ) and corresponding spin-asymmetry data as a function of  $\theta$  around normal incidence, measured with three counters C1, C2, and C3 at different photon takeoff angles as sketched in the upper part of the figure.

the observation that the photon detection angle influences the experimental outcome significantly. We focus our attention on small angles around normal electron incidence (nonshaded area in Fig. 3), i.e., around  $\bar{\Gamma}$  in momentum space. The *integral* spin-asymmetry value within the interval  $-5^{\circ} < \theta < +5^{\circ}$  vanishes for C2 [ $A = (0.3 \pm 0.8)\%$ ]. In contrast, the value is clearly positive with  $A = (4.2 \pm 0.8)\%$  for C1 and negative with  $A = (-3.7 \pm 0.4)\%$  for C3. The data for C3 underline the observation of Fig. 2(c), where excess spin-down intensity was detected around normal electron incidence. The symmetric behavior of C2 is confirmed by spin-dependent parabolic fits (blue and red lines in Fig. 3), shifted in  $\theta$  and intersecting at  $\theta = 0$ . The tendency of the absolute value of  $A$  being smaller for C3 than for C1 may originate from the fact that C3 is in a position of lower symmetry compared with C1.

Our results show that the IPE intensity for SS at normal electron incidence, where SS has no intrinsic spin polarization, shows nonzero spin asymmetry for certain photon-detection geometries. The result of nonzero spin asymmetry around normal electron incidence obtained with counter C3 in Fig. 2(c) is neither a consequence of insufficient statistics nor incorrect alignment of the sample. In contrary, the spin asymmetry does not change significantly for a few degrees around normal electron incidence. As a consequence,

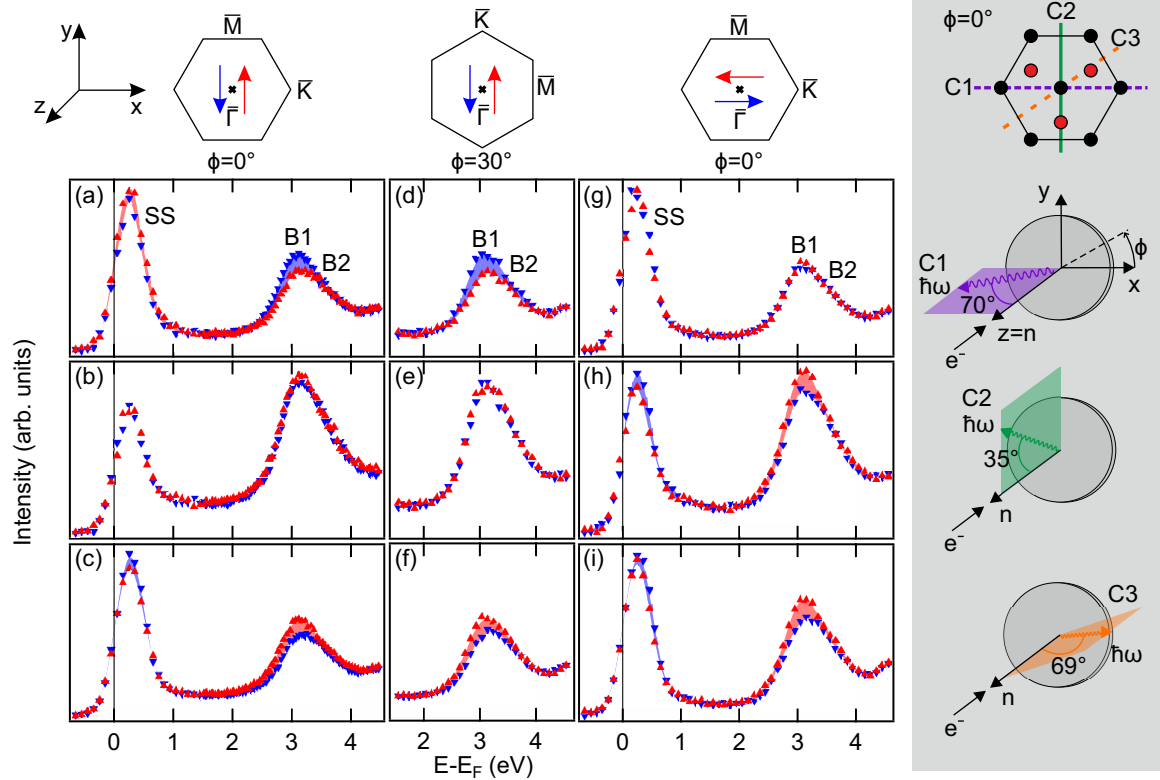


FIG. 4. Spin-resolved IPE spectra of Re(0001) at normal electron incidence for different configurations of electron spin polarization, sample orientation, and photon detection angle: (a)–(c) spin polarization  $P_y$  parallel  $\bar{\Gamma}\bar{M}$ , (d)–(f)  $P_y$  parallel  $\bar{\Gamma}\bar{K}$ , and (g)–(i)  $P_x$  parallel  $\bar{\Gamma}\bar{K}$ . The spectra in (a), (d), and (g) have been measured with counter C1, (b), (e), and (h) with counter C2, (c), (f), and (i) with counter C3. The various sample and spin-polarization geometries are sketched in the upper part of the figure; the counter geometries are displayed in the gray-shaded part.

a small misalignment in  $\theta$  is tolerable without changing the results. The observed effect is rather a consequence of lowering the symmetry of the experiment by detecting the photons in selected directions. The different geometries enter the transition matrix elements, even in our case of detecting unpolarized light.

To dig deeper into this phenomenon, we extended our measurements to the bulk-derived states B1 and B2 as well as to further experimental geometries: rotation of the sample and rotation of the spin polarization. All measurements were obtained for normal electron incidence within experimental uncertainty of  $\pm 2^\circ$ . In Fig. 4, we present a matrix of spin-resolved IPE spectra. The first column (a) to (c) contains spectra with spin polarization in  $y$  direction parallel to  $\bar{\Gamma}\bar{M}$  ( $P_y$ ). For taking the spectra of the second column (d) to (f), we rotated the sample by  $\phi = 30^\circ$ , i.e.,  $P_y$  is now parallel to  $\bar{\Gamma}\bar{K}$ . In the spectra of the third column (g) to (i), the sample was rotated back but the spin polarization was rotated by  $90^\circ$ , i.e.,  $P_x$  is parallel to  $\bar{\Gamma}\bar{K}$ . The three rows of the spectra matrix in Fig. 4 present data for the three different counters C1, C2, and C3. The various sample and spin-polarization geometries are sketched in the upper part of the figure, while the counter geometries are illustrated in the gray-shaded part on the right-hand side.

For SS, we find in the first column (a) to (c) the already described behavior: spin-up, zero, and spin-down asymmetry

for C1, C2, and C3, respectively. However, after rotation of the spin polarization, the situation has changed. We find in (g) to (i) zero, spin-down, and spin-down asymmetry for C1, C2, and C3, respectively. Note that C3 is  $32^\circ$  out of the measuring plane. We want to point out that the behavior of B1 is found inverted compared with SS: Where the asymmetry of SS favors spin-up, B1 shows spin-down asymmetry and vice versa. In the cases of zero spin asymmetry, this is true for both SS and B1. In addition, we tested a sample rotation by  $30^\circ$  with no change at all on the spin asymmetry for B1, shown in the second column of Figs. 4(d)–4(f). Remarkably, B2 does not show any spin asymmetry, independent of the direction of spin polarization and/or sample geometry.

Summarizing our observations based on the spectra in Fig. 4, we detect spin-polarization effects in IPE data for intrinsically unpolarized states, taken at normal electron incidence. This effect does not depend on the sample orientation but on the relative orientation of electron spin polarization and photon-detection direction. In cases, where the spin polarization lies parallel to the plane of photon detection and electron incidence, no spin asymmetry is detected. In all other cases, a nonzero spin asymmetry can be detected which is opposite in sign for the surface state SS and the bulk-derived state B1. No spin asymmetry is observed for B2.

Based on our electronic structure calculations (see Fig. 1) we calculated IPE spectra as described in Sec. III for the

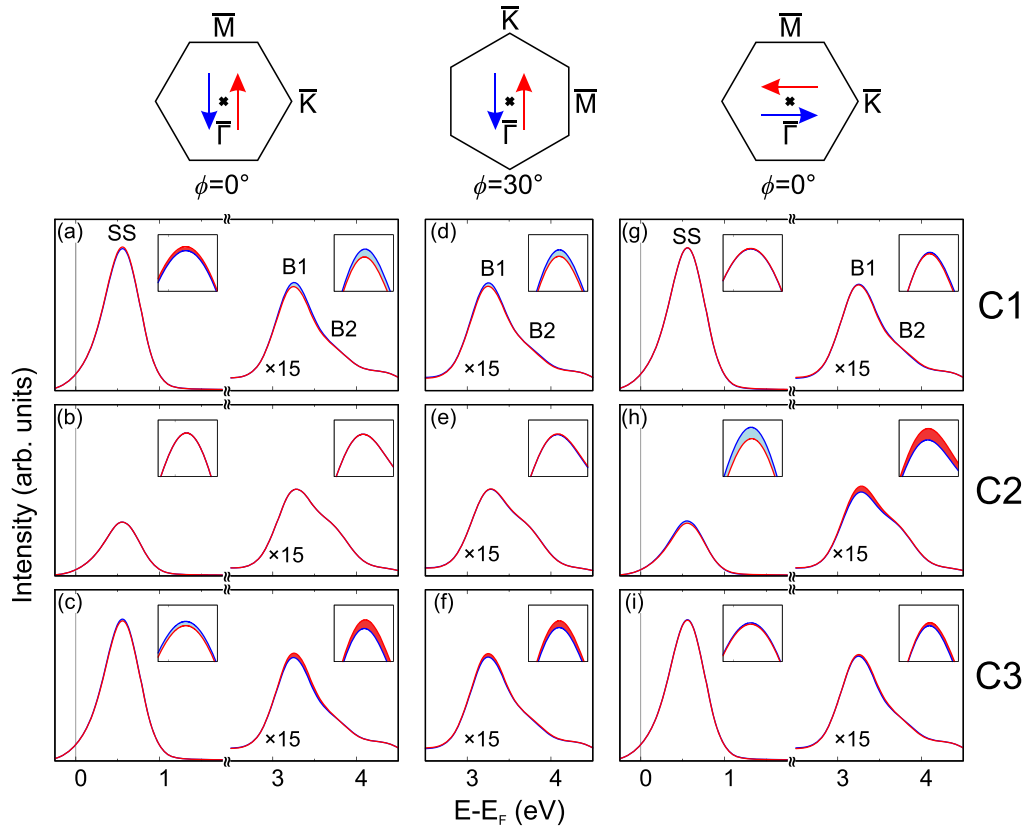


FIG. 5. Calculated IPE spectra of Re(0001) for normal electron incidence. A broadening of 400 meV is employed. The configurations of electron spin polarization, sample orientation and photon detection angle are the same as in Fig. 4.

various experimental geometries concerning electron spin polarization, sample orientation, and photon detection angle. The photon counters used in the IPE experiments average over all components of the vector potential which are perpendicular to the direction of photon propagation. To consider this fact, the intensities in Fig. 5 resulting from Eq. (1) are averaged accordingly [43]. The calculated IPE spectra are displayed in Fig. 5, which is organized identically to the matrix of experimental spectra in Fig. 4. Note that the intensities above 2.5 eV which comprise B1 and B2 are enlarged by a factor of 15 compared to those at lower energies. The insets show enlargements of the peak maxima to highlight the intensity differences between spin up and spin down.

A comparison between experiment and theory shows that all experimental findings are supported by the calculations: (i) the existence/nonexistence of spin asymmetry as well as its sign depending on the experimental geometry, (ii) the reversed sign of the spin asymmetry for SS and B1, (iii) the observation of spin asymmetry for SS and B1 but not for B2. Quantitative differences are found with respect to state energies, IPE intensities between SS and B1,2 as well as the size of spin differences. The first is attributed to deficiencies of the DFT-LDA approach, which is known to often overestimate the bandwidths in metals [44,45]. Concerning the latter differences, we can only speculate. According to Fig. 1(b), the density of states for SS and B1,2 are comparable in contrast to the calculated IPE intensities. This may be caused by transition probabilities from initial states, which are calculated based on a surface barrier taken from the self-consistently derived

potential. This may lead to uncertainties in the initial states above the vacuum level. Obviously, in the calculation, the intensity of  $p_z$ -derived states is overestimated. This effect may also be responsible for the calculated smaller spin differences than in experiment.

Experiment and theory agree in the observation of spin-dependent off-normal photon emission from transitions into intrinsically unpolarized states at  $\bar{\Gamma}$ . Note that no polarization analysis of the emitted photons was necessary to observe this phenomenon. To understand this effect, we have to consider the symmetry of the states. A corresponding effect has been reported for photoemission: normal emission of spin-polarized electrons excited by unpolarized light impinging off-normally on nonmagnetic cubic (111) surfaces [5,6]. Since the symmetry of the bands normal to cubic (111) surfaces is the same as normal to an hcp(0001) surface, namely  $\Lambda$ , we can transfer this analysis to our results on Re(0001). In the former studies, spin-orbit-induced hybridization of states was identified as the main cause.  $\Lambda_6^1\Lambda_6^3$  hybrids were involved in the transitions, where spin-polarized electrons were emitted. No azimuthal rotation dependence was predicted for initial states of double-group symmetry  $\Lambda_6$ . For states of  $\Lambda_{4+5}$  symmetry, a spin-orbit-induced spin-polarization effect is also predicted, yet with azimuthal rotation dependence. However, it is partially canceled for unpolarized light. In addition, in our case with a sixfold symmetry of the surface due to steps and terraces as described above, the spin-polarization effect for  $\Lambda_{4+5}$  states is expected to vanish (see Fig. 1 in Ref. [5]).

In the following, we apply this concept to our results for SS, B1, and B2. B2 has predominantly  $\Lambda_{4+5}$  symmetry. As a consequence, we do not expect considerable spin asymmetry in the IPE spectra, in agreement with our theoretical and experimental results. SS and B1 are  $\Lambda_6^1\Lambda_6^3$  hybrids with different ratios of the two components. The  $\Lambda_{4+5}$  contributions are energy degenerate but do not hybridize with the  $\Lambda_6$  bands. An IPE final state  $\psi_f$  corresponding to such a hybrid is degenerate with the time-reversed state  $\tilde{\psi}_f$ . Transitions from an initial state  $\psi_i^+$  (which is outside the crystal a plane wave) with a spin polarization + (given by the experimental setup) to  $\psi_f$  and  $\tilde{\psi}_f$  on the one hand, and from an initial state  $\psi_i^-$  with an opposite spin orientation to the same final states otherwise, can occur with different probabilities. This results from the fact that  $\psi_i^+$  and  $\psi_i^-$  are not time reversed with respect to each other because only *incoming* waves are involved in the IPE process.

Due to the symmetry of the transition-matrix elements for  $\Lambda_6^1$  and  $\Lambda_6^3$  basis functions, a spin-polarization effect results that does not depend on the sample orientation and where the spin polarization is perpendicular to the direction of photon emission [5]. Furthermore, it changes its sign for photon detection from the opposite side. No spin asymmetry can be detected if electron spin polarization and the plane of photon emission are parallel. Maximum spin asymmetry is expected, if the electron spin polarization and plane of photon emission are perpendicular. Due to the individual contributions of  $\Lambda_6^1$  and  $\Lambda_6^3$  (size and sign) to the hybridized states SS and B1, the transition matrix elements lead to different spin-asymmetry effects, which are—in our case—opposite in sign. All predictions described above are verified in our data:

(i) spin asymmetry for SS and B1 but not for B2, (ii) spin asymmetry with opposite sign for C1 and C3, none for C2 [Figs. 4(a)–4(f)], (iii) no change of the spin asymmetry for azimuthal rotation of the sample [Figs. 4(d)–4(f)], and (iv) change of spin asymmetry after rotation of the electron spin polarization [Figs. 4(g)–4(i)]. Note that the spin asymmetry does not vanish in the configuration shown in Fig. 4(i) due to the oblique counter position.

## V. CONCLUSION

We investigated the unoccupied electronic structure of Re(0001) around  $\bar{\Gamma}$  by spin- and angle-resolved inverse photoemission, experimentally and theoretically. A crystal-induced surface state SS just above the Fermi level, an image-potential-induced surface state IS below the vacuum level, and two bulk-derived bands B1 and B2 were identified. SS, which is a hole pocket just around  $\bar{\Gamma}$ , shows a Rashba-type spin texture. The spectra for SS and B1 at normal electron incidence show considerable spin asymmetry, although the states are intrinsically unpolarized. Based on a comprehensive experimental and theoretical study for various geometries concerning electron spin polarization, photon-detection direction, and sample orientation, the observed spin-dependent photon emission was traced back to spin-orbit-induced hybridization of the involved electron states.

## ACKNOWLEDGMENTS

It is a pleasure to thank J. Braun, J. Henk, M. Holtmann, and J. Minár for fruitful discussions.

- 
- [1] R. Feder, *Polarized Electrons in Surface Physics* (World Scientific, Singapore, 1995).
- [2] U. Heinzmann and J. H. Dil, Spin-orbit-induced photoelectron spin polarization in angle-resolved photoemission from both atomic and condensed matter targets, *J. Phys.: Condens. Matter* **24**, 173001 (2012).
- [3] T. Okuda and A. Kimura, Spin- and angle-resolved photoemission of strongly spin-orbit coupled systems, *J. Phys. Soc. Jpn.* **82**, 021002 (2013).
- [4] M. Donath, In or out of control? Electron spin polarization in spin-orbit-influenced systems, *Encyclopedia of Interfacial Chemistry: Surface Science and Electrochemistry*, 131 (2018).
- [5] E. Tamura and R. Feder, Spin-polarized normal photoemission from non-magnetic (111)-surfaces by p-polarized light, *Solid State Commun.* **79**, 989 (1991).
- [6] B. Schmiedeskamp, N. Irmer, R. David, and U. Heinzmann, A new spin effect in photoemission with unpolarized light: Experimental evidence of spin polarized electrons in normal emission from Pt(111) and Au(111), *Appl. Phys. A* **53**, 418 (1991).
- [7] J. Henk and R. Feder, Spin polarization in normal photoemission by linearly polarized light from non-magnetic (110) surfaces, *Europhys. Lett.* **28**, 609 (1994).
- [8] S. N. P. Wissing, A. B. Schmidt, H. Mirhosseini, J. Henk, C. R. Ast, and M. Donath, Ambiguity of Experimental Spin Information from States with Mixed Orbital Symmetries, *Phys. Rev. Lett.* **113**, 116402 (2014).
- [9] H. Wortelen, H. Mirhosseini, K. Miyamoto, A. B. Schmidt, J. Henk, and M. Donath, Tuning the spin signal from a highly symmetric unpolarized electronic state, *Phys. Rev. B* **91**, 115420 (2015).
- [10] K. Miyamoto, H. Wortelen, T. Okuda, J. Henk, and M. Donath, Circular-polarized-light-induced spin polarization characterized for the Dirac-cone surface state at W(110) with  $C_{2v}$  symmetry, *Sci. Rep.* **8**, 10440 (2018).
- [11] P. Eickholt, P. Krüger, S. D. Stolwijk, A. B. Schmidt, and M. Donath, Breaking time-reversal symmetry at the  $\bar{M}$  point: Spin signal from a surface state on Tl/Ge(111), *Phys. Rev. B* **101**, 165411 (2020).
- [12] Y. A. Bychkov and E. I. Rashba, Properties of a 2D electron gas with lifted spectral degeneracy, *Pis'ma Zh. Eksp. Teor. Fiz.* **39**, 66 (1984) [*JETP Lett.* **39**, 78 (1984)].
- [13] S. LaShell, B. A. McDougall, and E. Jensen, Spin Splitting of an Au(111) Surface State Band Observed with Angle Resolved Photoelectron Spectroscopy, *Phys. Rev. Lett.* **77**, 3419 (1996).
- [14] G. Nicolay, F. Reinert, S. Hübner, and P. Blaha, Spin-orbit splitting of the L-gap surface state on Au(111) and Ag(111), *Phys. Rev. B* **65**, 033407 (2001).
- [15] M. Hoesch, M. Muntwiler, V. N. Petrov, M. Hengsberger, L. Patthey, M. Shi, M. Falub, T. Greber, and J. Osterwalder, Spin

- structure of the Shockley surface state on Au(111), *Phys. Rev. B* **69**, 241401(R) (2004).
- [16] S. N. P. Wissing, C. Eibl, A. Zumbülte, A. B. Schmidt, J. Braun, J. Minár, H. Ebert, and M. Donath, Rashba-type spin splitting at Au(111) beyond the Fermi level: The other part of the story, *New J. Phys.* **15**, 105001 (2013).
- [17] H. Wortelen, K. Miyamoto, H. Mirhosseini, T. Okuda, A. Kimura, D. Thonig, J. Henk, and M. Donath, Spin-orbit influence on  $d_{z^2}$ -type surface state at Ta(110), *Phys. Rev. B* **92**, 161408(R) (2015).
- [18] B. Engelkamp, H. Wortelen, H. Mirhosseini, A. B. Schmidt, D. Thonig, J. Henk, and M. Donath, Spin-polarized surface electronic structure of Ta(110): Similarities and differences to W(110), *Phys. Rev. B* **92**, 085401 (2015).
- [19] R. H. Gaylord and S. D. Kevan, Spin-orbit-interaction-induced surface resonance on W(011), *Phys. Rev. B* **36**, 9337(R) (1987).
- [20] K. Miyamoto, A. Kimura, K. Kuroda, T. Okuda, K. Shimada, H. Namatame, M. Taniguchi, and M. Donath, Spin-Polarized Dirac-Cone-Like Surface State with  $d$  Character at W(110), *Phys. Rev. Lett.* **108**, 066808 (2012).
- [21] D. Thonig, T. Rauch, H. Mirhosseini, J. Henk, I. Mertig, H. Wortelen, B. Engelkamp, A. B. Schmidt, and M. Donath, Existence of topological nontrivial surface states in strained transition metals: W, Ta, Mo, and Nb, *Phys. Rev. B* **94**, 155132 (2016).
- [22] H. J. Elmers, J. Regel, T. Mashoff, J. Braun, S. Babenkov, S. Chernov, O. Fedchenko, K. Medjanik, D. Vasilyev, J. Minar, H. Ebert, and G. Schönhense, Rashba splitting of the Tamm surface state on Re(0001) observed by spin-resolved photoemission and scanning tunneling spectroscopy, *Phys. Rev. Research* **2**, 013296 (2020).
- [23] M. Donath, Spin-dependent electronic structure at magnetic surfaces: The low-Miller-index surfaces of nickel, *Surf. Sci. Rep.* **20**, 251 (1994).
- [24] S. D. Stolwijk, H. Wortelen, A. B. Schmidt, and M. Donath, Rotatable spin-polarized electron source for inverse-photoemission experiments, *Rev. Sci. Instrum.* **85**, 013306 (2014).
- [25] C. Thiede, I. Niehues, A. B. Schmidt, and M. Donath, The acetone bandpass detector for inverse photoemission: Operation in proportional and Geiger–Müller modes, *Meas. Sci. Technol.* **29**, 065901 (2018).
- [26] H. Wortelen, J. Henk, and M. Donath, Spin-orbit and anisotropy effects in unoccupied bulk, surface, and image-potential states on W(110), *Phys. Rev. B* **95**, 085416 (2017).
- [27] A. Zumbülte, A. B. Schmidt, and M. Donath, Momentum resolution in inverse photoemission, *Rev. Sci. Instrum.* **86**, 013908 (2015).
- [28] S. Ouazi, T. Pohlmann, A. Kubetzka, K. von Bergmann, and R. Wiesendanger, Scanning tunneling microscopy study of Fe, Co and Cr growth on Re(0001), *Surf. Sci.* **630**, 280 (2014).
- [29] J. P. Perdew and A. Zunger, Self-interaction correction to density-functional approximations for many-electron systems, *Phys. Rev. B* **23**, 5048 (1981).
- [30] B. Stärk, P. Krüger, and J. Pollmann, Magnetic anisotropy of thin Co and Ni films on diamond surfaces, *Phys. Rev. B* **84**, 195316 (2011).
- [31] L. Kleinman and D. M. Bylander, Efficacious Form for Model Pseudopotentials, *Phys. Rev. Lett.* **48**, 1425 (1982).
- [32] L. A. Hemstreet, C. Y. Fong, and J. S. Nelson, First-principles calculations of spin-orbit splittings in solids using nonlocal separable pseudopotentials, *Phys. Rev. B* **47**, 4238 (1993).
- [33] H. J. Monkhorst and J. D. Pack, Special points for Brillouin-zone integrations, *Phys. Rev. B* **13**, 5188 (1976).
- [34] A. Urru and A. Dal Corso, Spin-polarized electronic surface states of Re(0001): An ab-initio investigation, *Surf. Sci.* **686**, 22 (2019).
- [35] R. W. G. Wyckoff, *Crystal structures I* (Wiley, New York, 1963).
- [36] H. L. Davis and D. M. Zehner, Preliminary LEED analysis of the clean Re(0001) surface, *Bull. Am. Phys. Soc.* **24**, 468 (1979).
- [37] J. P. Perdew, J. A. Chevary, S. H. Vosko, K. A. Jackson, M. R. Pederson, D. J. Singh, and C. Fiolhais, Atoms, molecules, solids, and surfaces: Applications of the generalized gradient approximation for exchange and correlation, *Phys. Rev. B* **46**, 6671 (1992).
- [38] The orbitals are localized at the fictitious positions of a Re crystal in that half space.
- [39] P. A. Khomyakov, G. Brocks, V. Karpan, M. Zwierzycki, and P. J. Kelly, Conductance calculations for quantum wires and interfaces: Mode matching and Green’s functions, *Phys. Rev. B* **72**, 035450 (2005).
- [40] F. Huerkamp, P. Krüger, and J. Pollmann, Investigation of electron transmission through Co/C/Co magnetic tunnel junctions, *Phys. Rev. B* **89**, 125302 (2014).
- [41] M. S. Hybertsen and S. G. Louie, Electron correlation in semiconductors and insulators: Band gaps and quasiparticle energies, *Phys. Rev. B* **34**, 5390 (1986).
- [42] M. Donath and V. Dose, Temperature behaviour of a “magnetic” band in nickel, *Europhys. Lett.* **9**, 821 (1989).
- [43] To this end, we compute  $I(\mathbf{A}, \mathbf{S})$  for 24 equidistant orientations of  $\mathbf{A}$ , all of them orthogonal to the axis of the photon detector.
- [44] I.-W. Lyo and E. W. Plummer, Quasiparticle Band Structure of Na and Simple Metals, *Phys. Rev. Lett.* **60**, 1558 (1988).
- [45] C. Friedrich, S. Blügel, and A. Schindlmayr, Efficient implementation of the GW approximation within the all-electron FLAPW method, *Phys. Rev. B* **81**, 125102 (2010).